



HAL
open science

Understanding the Structural and Electronic Properties of Photoactive Tungsten Oxide Nanoparticles from Density Functional Theory and GW Approaches

Valentin Diez-Cabanes, Ángel Morales-García, Francesc Illas, Mariachiara Pastore

► **To cite this version:**

Valentin Diez-Cabanes, Ángel Morales-García, Francesc Illas, Mariachiara Pastore. Understanding the Structural and Electronic Properties of Photoactive Tungsten Oxide Nanoparticles from Density Functional Theory and GW Approaches. *Journal of Chemical Theory and Computation*, 2021, 17 (6), pp.3462-3470. 10.1021/acs.jctc.1c00293 . hal-03421131

HAL Id: hal-03421131

<https://hal.science/hal-03421131>

Submitted on 9 Nov 2021

HAL is a multi-disciplinary open access archive for the deposit and dissemination of scientific research documents, whether they are published or not. The documents may come from teaching and research institutions in France or abroad, or from public or private research centers.

L'archive ouverte pluridisciplinaire **HAL**, est destinée au dépôt et à la diffusion de documents scientifiques de niveau recherche, publiés ou non, émanant des établissements d'enseignement et de recherche français ou étrangers, des laboratoires publics ou privés.



Distributed under a Creative Commons Attribution 4.0 International License

Understanding the Structural and Electronic Properties of Photoactive Tungsten Oxide (WO_3) Nanoparticles from DFT and GW approaches

Valentin Diez-Cabanes,^{1,*} Ángel Morales-García,^{2,*} Francesc Illas,² Mariachiara Pastore^{1,*}

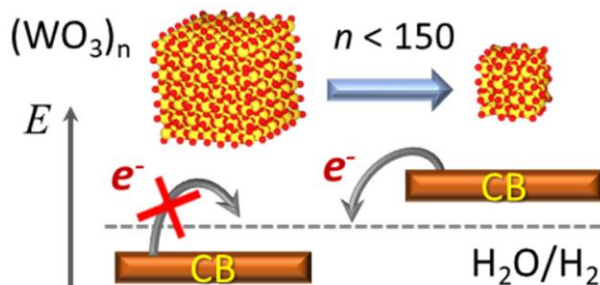
¹ Université de Lorraine & CNRS, Laboratoire de Physique et Chimie Théoriques (LPCT), UMR 7019, F-54000, Nancy, France

² Departament de Ciència de Materials i Química Física & Institut de Química Teòrica i Computacional (IQTCUB), Universitat de Barcelona, c/Martí i Franqués 1-11, 08028 Barcelona, Spain

*Authors to whom correspondence should be addressed: valentin.diez-cabanes@univ-lorraine.fr; angel.morales@ub.edu; mariachiara.pastore@univ-lorraine.fr

KEYWORDS tungsten oxide nanoparticles, quantum confinement, photocatalysis, GW approximation

TOC Figure:



ABSTRACT

Tungsten trioxide (WO_3) derived nanostructures have emerged recently as feasible semiconductors for photocatalytic purposes due to their visible light harvesting that overcomes the drawbacks presented by TiO_2 derived nanoparticles (NPs). However, applications are still limited by the lack of fundamental knowledge at nanoscale due to the poor knowledge of the physical processes that affect to their photoactivity. To fill this gap, we report here a detailed computational study using a combined Density Functional Theory (DFT)- GW scheme to investigate the electronic structure of realistic WO_3 NPs containing up to 1680 atoms. Different phases and morphologies are considered so as to provide reliable structure-property relationships. Upon the proper benchmark of our DFT- GW methodology, we use this highly accurate approach to establish relevant rules for the design of photoactive WO_3 nanostructures by pointing out the most stable morphologies at the nanoscale and the appropriate size regime at which the photoactive efficiency is enhanced.

Introduction

Heterogenous photocatalytic water splitting represents one of the most attractive technologies, since only photons with the appropriate energy are required to drive the solar-to-chemical energy conversion.¹ The first step of this process is the light absorption by the photoactive semiconductor to form electron-hole pairs, which have to fast and efficiently migrate toward the surface of the catalyst, where water molecules are reduced/oxidized by the electrons/holes to form H_2/O_2 . A visible-light-driven photocatalyst must exhibit an energy gap below 3.0 eV. The design of such photocatalyst is fundamental to guarantee an optimal visible-light absorption. In principle, this requires a deep knowledge of structure-property relationships, which allow one

monitoring the optical and electronic properties by engineering of size and morphology of the nanoparticles (NPs). As a matter of fact, the design of NPs with diameters below 5 nm via facet engineering² is one of the most promising avenues to improve the photocatalytic activity. At this size the effects of the quantum confinement facilitate the transfer of charge carriers.^{3,4} This implies that the size and morphology of NPs are two important factors in determining their electronic structure and, hence, their potential use as photocatalysts.⁵ The effect of the structural features can be phenomenologically observed by experiments but a deep understanding, and more importantly, a systematic rationalization of the structure-property relationships is not straightforward and requires relying on large-scale atomistic simulations based on accurate theoretical methods and realistic structural models.⁶⁻⁸ In this context, setting up a reliable but still affordable methodology capable to deliver accurate information on the structure, the stability and the band-edge offsets of realistic nanocrystals is crucial for the design of efficient NPs for photocatalytic applications.⁹ A proper modelling of NPs usually implies to tackle two main issues: (i) the construction of suitable structural models at the atomistic scale that are able to capture both the effects of morphology and size, which is often done by following top-down or bottom-up approaches; and (ii) the setup of a high precise and unbiased approach which can be employed to determine the electronic properties of NPs at the nanoscale level within an affordable computational cost.

TiO₂ NPs constitute by far the most studied photocatalytic material,^{10,11} although the need for UV radiation makes it inappropriate for large scale water splitting applications. In this context, WO₃ derived nanostructures have emerged as promising photocatalytic materials due to their Earth abundancy, low cost, harmlessness, suitable band edge energies for water splitting reactions, and high chemical stability, even in the presence of strong oxidizing conditions,

making them relevant for many technological applications.¹² More importantly, the experimental band gap energy (E_g) of bulk WO_3 is in the 2.5-3.0 eV range,^{13,14} sensibly smaller than the corresponding value for bulk TiO_2 which is in the 3.0-3.2 eV range.¹⁵ WO_3 can, thus, act as visible light-driven photocatalyst. However, a systematic and fundamental knowledge of its photoactivity as a function of morphology and size is still lacking. This motivated us to carry out this study, since most of reported studies dealing with the modelling of WO_3 materials have focused either on the bulk¹⁶⁻¹⁹ or on extended surfaces.²⁰⁻²² There are also studies regarding very small $(\text{WO}_3)_3$ nanoclusters (NCs)^{23,24} but till the date, the modelling of realistic WO_3 NPs is still missing. To fill this gap, we have followed the successfully computational strategy set up by some of us for TiO_2 ²⁵⁻²⁷ and ZnO ²⁸ nanostructures, which permitted us to design different morphologies for a given composition or to vary the composition for a certain given morphology.

Concerning the choice of the proper level of theory, GW formalism (G represents the time-ordered one-body Green's function, while W depicts the screened Coulomb potential) has attracted the attention of both Physics and Chemistry communities during the last years due to its excellent performance in terms of accuracy and computational cost, which is inherent of its N^3 scalability (being N the number of atoms of the system under study).²⁹ Notably, this perturbative method confirmed as appropriate method to study the electronic properties of medium size TiO_2 ³⁰⁻³² and small transition metal nanostructures.³³ Nonetheless, due to the large number of atoms in our realistic WO_3 nanostructures (>1500), for the largest systems only standard DFT methods (i.e. Local Density Approximation (LDA) or Generalized Gradient Approximation (GGA)) are applicable, which clearly translates into a larger dependence on the choice of the exchange-correlation potential with a possible significant loss of accuracy. Here we overcome

such limitation by establishing a combined DFT-*GW* protocol, relying on the correlation between the DFT and the *GW* results within a representative subset of nanoparticles, spanning all the examined morphologies. This enables us to predict the properties of a complete set of WO₃ nanostructures from few cluster units to realistic NPs (up to 1680 atoms) at a higher level of accuracy.

In this work, we discuss the merits and limitations of our combined *GW*-DFT method and its implications in the design of WO₃ NPs for photocatalysis. We first address the evolution of the relative stability of the WO₃ NPs with respect to their size by considering different structural families and the most likely morphology at the lowest dimension scale. Next, we benchmark the electronic structure properties of these particles on the basis of the total variational energy differences (Δ SCF) to evaluate the suitability of our *GW* based methodology. Finally, we use our DFT-*GW* approach to assess the evolution of the NPs energetic levels with respect to their size with the ultimate goal of pointing out the optimal combinations of size and morphology to enhance the photoactivity of the material.

Models and methods

Definition of the structural models

The present WO₃ NPs are all stoichiometric and have been designed by using the top-down approach.³⁴ Our study involves NPs sizing from \square 0.4 to \square 5 nm, well representing the size range of the smallest synthesized NPs found in the literature (0.7- 5 nm),³⁵⁻³⁹ exhibiting cubic, rectangular, octahedral, spherical, hexagonal nanosheet and cuboid nanowires morphologies; as depicted in Figure 1.

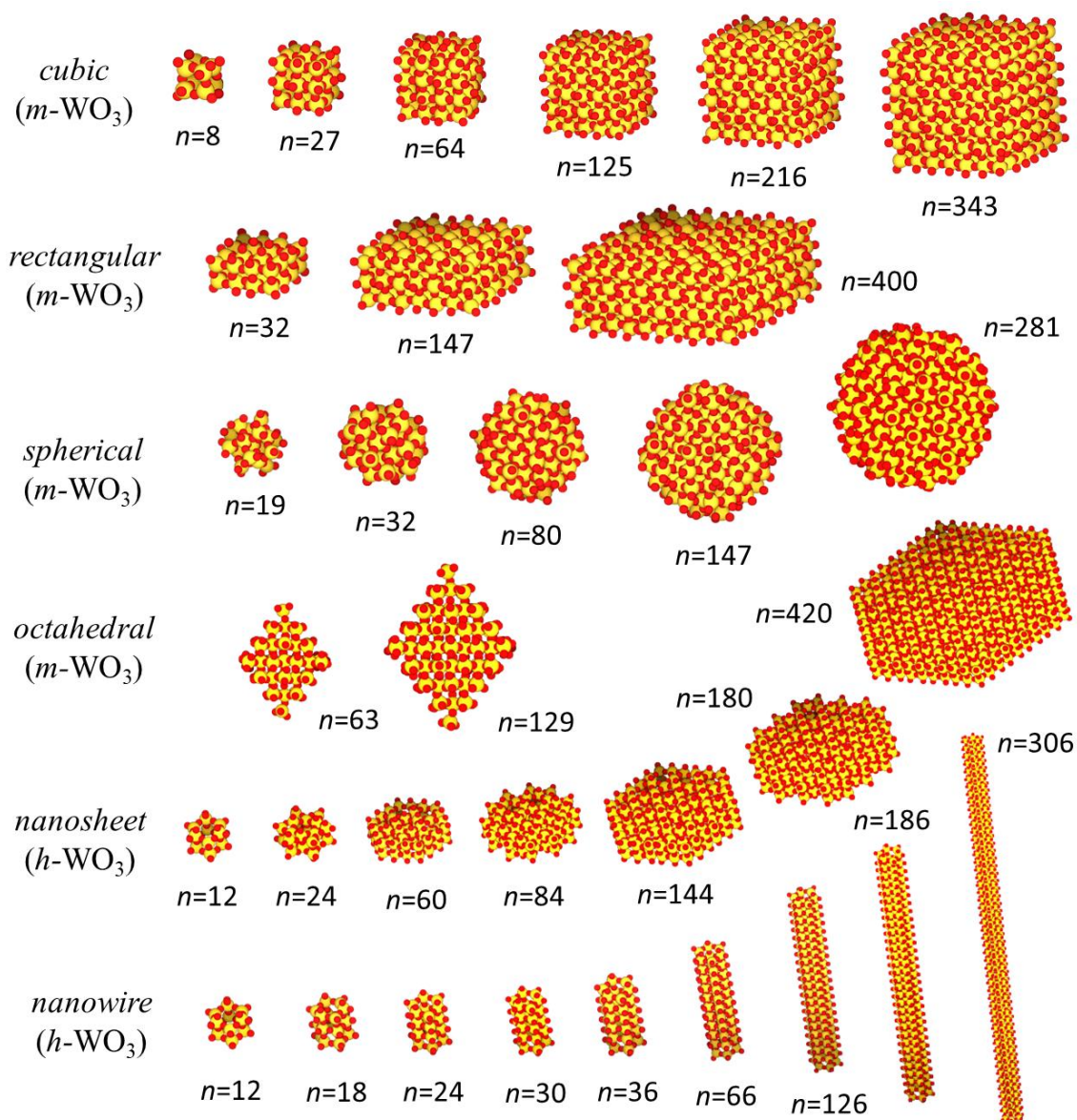


Figure 1. The full set of WO₃ NPs with different sizes and morphologies investigated here.

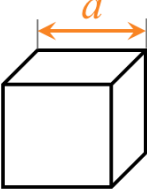
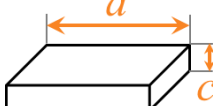
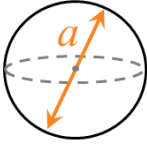
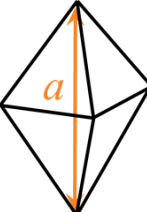
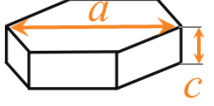

These nanostructures are generated by considering the monoclinic (m-WO₃) and hexagonal (h-WO₃) bulk phases with their experimentally determined preferential exposed facets. Cubic and rectangular WO₃ NPs are obtained from the monoclinic bulk phase exposing the (200), (020) and (002) surfaces.^{40,41} More in detail, the rectangular NPs are built following the structural features previously reported, with the (002) surface being the preferential one with respect to the (200)

and (020) surface.⁴¹ Octahedral WO_3 NPs are designed by cutting the $m\text{-WO}_3$ along the (111) directions.⁴² For the particular case of the spherical NPs, these nanostructures are obtained by imposing symmetrical cuts (non-symmetric nanostructures were found to be unstable upon relaxation) to the monoclinic bulk phase along several directions, thus resulting in a polyhedral ‘spherical-like’ shape nanostructure. Regarding the hexagonal nanosheets, the (001) surface is conserved according to previously reported works.^{43,44} On the other hand, the hexagonal nanowires expose the (110) surfaces as found in experiments, thus resulting in a cuboid prismatic-shaped structure.^{43,44}

In the present study we also include the exposed (100) and (010) surfaces with the aim of getting stoichiometric and symmetric nanowires with a section involving the lowest possible area, thus leading to a prismatic nanostructure with a hexagonal moiety. Note that cuboid prismatic 1D nanostructures with the exposed (110) surface have also been tested but all were found to be unstable upon geometry optimization. Once the nanostructures exposing the desired surfaces have been built, we systemically modify the number oxygen surface atoms, keeping the same coordination for all superficial chemical units, to obtain a quasi-stoichiometric symmetric nanostructures. Finally, once this symmetric structure is relaxed, we symmetrically add or remove certain oxygen surface atoms to preserve the stoichiometry of the system, prior to the final relaxation of the nanostructure. It is noteworthy to mention that we have selected those relaxed nanostructures which exhibited the larger stability and non-metallic behaviour among different candidates, thus reducing the randomness in the construction of our models. In addition, we are aware that the surface geometries of the pristine nanostructures may be slightly modified by the presence of the solvent molecules around the NP surface with a fraction being probably

dissociated. Nonetheless, the investigation of the interaction between the solvent and the NPs is beyond the scope of the present paper, and it will be the motivation for prospective works.

Table 1. Number of WO_3 units (n) and geometrical parameters for all NPs studied in this work, as they are depicted in the schemes on the left side of the Table. The R factor corresponds to the ratio between the largest and the lowest dimensions of the NP.

Parameters	NP	n	a (nm)	c (nm)	R	V (nm ³)
	cubic	8	0.4	-	-	0.06
		27	0.8	-	-	0.51
		64	1.2	-	-	1.73
		125	1.6	-	-	4.1
		216	2.0	-	-	8
		343	2.4	-	-	13.82
	rectangular	32	1.2	0.4	3	0.58
		147	2.4	0.8	3	4.61
		400	3.6	1.2	3	15.55
	spherical	19	0.8	-	-	0.27
		32	1.6	-	-	2.14
		57	2.0	-	-	4.19
	octahedral	147	2.7	-	-	10.31
		281	3.5	-	-	22.45
		63	2.3	-	-	2.22
	nanosheet	129	3.2	-	-	5.03
		12	0.7	0.4	1.8	0.13
		24	1.2	0.4	3.0	0.37
		60	2.2	0.4	5.5	1.26
		84	2.6	0.4	6.5	1.76
		144	3.7	0.4	9.3	3.56
	nanowire	180	4.1	0.4	10.3	4.37
		420	6.8	0.4	17.1	11.57
		12	0.7	0.4	1.8	0.13
		18	0.7	0.8	1.1	0.25
		24	0.7	1.1	1.6	0.35
		30	0.7	1.5	2.1	0.48
		36	0.7	1.9	2.7	0.60
		66	0.7	3.8	5.4	1.21
		126	0.7	7.6	10.9	2.42
		186	0.7	11.1	15.9	3.53
306	0.7	19.1	27.3	6.08		

For each one of the structures shown in Figure 1, geometry optimization was carried out in the framework of Density Functional Theory (DFT) using the Perdew-Burke-Ernzerhof (PBE) functional,⁴⁵ including the Periodic Boundary Conditions (PBC) and employing a combination of Gaussian and plane wave basis set as implemented in CP2K package.⁴⁶ To avoid interactions between periodically repeated images of the NPs, the size of the unit cell was set to assure a minimum vacuum distance of 15 Å between neighbouring nanostructures. The calculations were carried out with a Double-zeta Valence Polarized (DZVP) and an energy cut-off for the auxiliary plane wave basis equal to 500 Ry, whereas the core electrons were described by means of Goedecker-Teter-Hutter (GTH) pseudopotentials.⁴⁷

Electronic structure calculations

The electronic properties of optimized structures were studied using an all-electron approach and employing a numerical atom-centered (NAO) orbital basis set. These calculations were carried out using the Fritz Haber Institute ab initio molecular simulations (FHI-AIMS) program package.⁴⁸ A light grid and tier-1 basis set is used, which lead to a similar quality to a valence triple- ζ plus polarization Gaussian Type Orbitals (GTO) basis set.²⁷ Due to the presence of heavy atoms such as W ($Z=74$), relativistic effects were accounted for through the zeroth order regular approximation (ZORA)^{49,50} to the Dirac equation, which has been shown to be accurate yet computationally affordable. We noted that relativistic effects were especially relevant for medium size NPs (see Figs. S1 and S2). For the sake of coherence with the level of theory employed for the geometry relaxation, electronic structure calculations were also carried out by using the GGA PBE and the hybrid PBE0⁵¹ at the PBE structure.

The lack of available experimental data to benchmark the electronic properties of small WO_3 NPs makes compulsory the adoption of highly accurate computational methods, which still allow to handle systems with hundreds of atoms, as the ones considered here. For that reason, semi-empirical approaches such as PBE+U have not been considered here in view of the absence of an experimental reference to properly set the values U parameter, which is responsible of preventing the excessive delocalization of the 5d W orbitals in the NP. In this context, the electron affinity (EA) and ionization potentials (IP) energies⁵² of the optimized NPs have been estimated by following three different approximation of increasing level of theory: *i*) the Kohn-Sham (KS) DFT energies,^{53,54} *ii*) the quasi-particle (QP) energies as obtained from many body perturbation theory (MBPT) based GW techniques,^{55,56} and, finally, *iii*) the Δ SCF method which provides the best possible estimated for a given density functional as it involves the difference of two variational energies. The GW technique is especially well suited for extended systems where Δ SCF become cumbersome due to the presence of charged states.

In the case of the KS energies, the IP/EA energies were taken directly from the values of the KS Highest/Lowest Occupied/Unoccupied Molecular Orbitals (HOMO/LUMO) energy levels with respect the vacuum level (VL). It is important to stress, however, that the equivalence between the fundamental gap (IP-EA) and the HOMO-LUMO KS gap strictly holds for the exact exchange and correlation functional⁵⁷ and that, in general, the frontier orbital E_g is significantly different, often smaller, than the experimental fundamental gap.⁵⁸ To predict more reliable E_g values for semiconductors, the most employed approach relies on the use of hybrid density functionals. These include a (moderate) fraction of Hartree-Fock exchange in the GGA or LDA standard exchange correlation (xc) density functional. By using hybrids functionals, one can correct the sizeable (30-40%) underestimation of E_g with respect to experiment^{59,60} by standard

LDA or GGA functionals.^{61,62} However, E_g appears to be extremely sensitive to the amount of Hartree-Fock exchange employed, and, in practice, one should always benchmark the calculated quantities against experimental data. For instance, for the monoclinic bulk WO_3 , the experimental gap is reproduced by including a 11% of non-local Hartree-Fock exchange (see Figure S3), which goes in line with the percentage reported in previous studies (15%),¹⁷ meaning that PBE0 (25%) is significantly overestimating this quantity by a ≈ 1.1 eV.

The second analysis consists of the GW method, which allows us accessing to the quasiparticle (QP) energies by perturbing the KS energy levels. In particular, two different approaches were used here: the one-shot GW approximation (G_0W_0) above mentioned and the more accurate eigenvalue partially self-consistent GW (ev GW), where the self-energy (Σ) is evaluated with partial self-consistency in the eigenvalues, while keeping the KS MO coefficients unchanged. The so-called G_0W_0 approach has been applied to a large dataset of molecular systems⁶³ with excellent agreement to experiments and also successfully applied to TiO_2 NPs.^{31,32} The GW calculations provide QP energies related to physical quantities, such as the electron injection/extraction energies, that can be directly compared with photoemission spectroscopy data.⁶⁴ Furthermore, GW techniques beyond G_0W_0 also present the advantage of providing QP energies which are less dependent on the amount of non-local exchange fraction in the starting DFT functional with respect to the KS energies.⁶⁵ For both GW approaches, we relied on a two pole fitting type for the analytical continuation of the self-energy, as it is implemented in the routines of FHI-AIMS.⁶⁶

Finally, in the variational ΔSCF method the IP/EA energies values were computed by employing the following formulas:

$$IP = E(N-1) - E(N) \quad (1)$$

$$EA = E(N) - E(N+1) \quad (2)$$

where $E(N)$, $E(N-1)$ and $E(N+1)$ correspond to the total energies for the neutral, +1 and -1 charged systems calculated at their equilibrium ground states (neutral) geometries. As it was the case of the one-shot G_0W_0 approximation, Δ SCF method may exhibit an important dependence of the initial KS energy orbitals, which depend on the density functional employed.

Results and discussion

Assessing the structural properties

The first property that we address is the energetic stability of WO_3 NPs as a function of their size, as summarized in Figure 2. Clearly, the octahedral NPs are less stable when compared to the other morphologies, thus confirming the experimentally assessed metastability of such NP.⁴² Accordingly, we have decided to discard this family of NPs in the following analysis. Regarding the rest of NPs belonging to the monoclinic bulk phase, a crossover around 50 units of WO_3 is found implying that, below this number, rectangular WO_3 NPs emerge as the most stable ones, whereas cubic WO_3 NPs ($a \approx 1$ nm, see Table 1) are energetically favoured for $n > 50$. Interestingly, cubic NPs reached an asymptotic behaviour in terms of energy for a relatively small number of WO_3 units ($n \approx 250$), meaning that for this type of morphology small sizes NPs ($a \approx 2.1$ nm) can be easily obtained without paying a high energy toll with respect to the bulk phase. Above the $n = 50$ crossover, the range of energies for the spherical NPs are found in the middle between the cubic and rectangular NP energies, while below this, the stability of these three families (cubic, rectangular, spherical) was found very similar. One can, thus, infer that

the effects of the morphology in the NP stability are especially relevant only for medium and large size NPs.

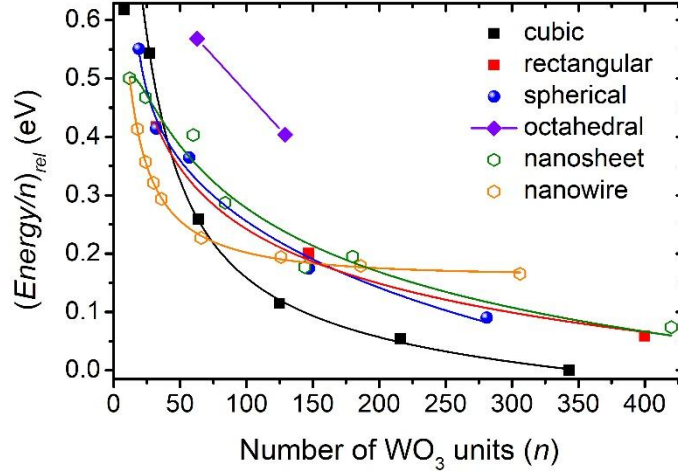


Figure 2. Ground state energies per chemical unit as function of the number of WO₃ units for the monoclinic cubic, rectangular, spherical, octahedral NPs and for the hexagonal nanosheets nanowires. We employed the Spherical Cluster Approximation (SCA)⁶⁷ to extract the fitting curves by following the fourth order expression: $E(n) = a_0 + a_1 * n^{-1/3} + a_2 * n^{-2/3} + a_3 * n^{-3/3} + a_4 * n^{-4/3}$

Moving to the derived hexagonal bulk phase NPs, while nanosheet NPs followed similar trends with respect to the monoclinic NPs, resulting in similar values for the asymptotic energies, nanowire NPs energies converged faster in terms of number of units ($n \square 125$). This family is, however, about 0.15 eV per unit less stable compared to the rest of NPs, as one may expect due to their 1D morphology, implying larger surface effects. In particular, we predicted that the stability of the nanowires as a function of their lengths already converges for ratios R around 11. Notably, we found a second crossover at $n = 165$ (which corresponds to R ratios of 9.8 and 14.2 for the nanosheet and nanowire WO₃ NPs, respectively). Nanowire and nanosheet structures are stable below and above such crossover.

Benchmarking the electronic structure methods: the effect of Hartree-Fock exchange

For the sake of illustration, we have taken the cubic $(\text{WO}_3)_8$ NP as reference system and we have estimated the IP and EA by using different level of approximations as the standard PBE and the hybrid PBE0 and PBEh50 density functionals, including 0%, 25% and 50% of Hartree-Fock exchange, respectively; the data are displayed in Figure 3.

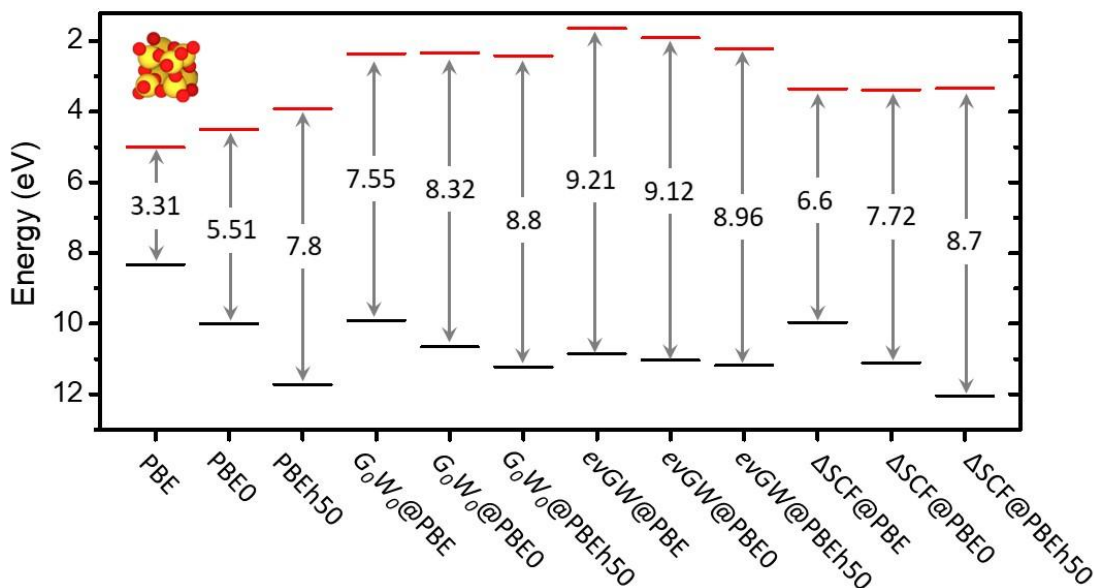


Figure 3. Difference between IP and EA for the monoclinic cubic $(\text{WO}_3)_8$ NPs as estimated by from KS orbital energies, G_0W_0 and evGW QPs and Δ SCF approaches, using PBE and modified PBE0 functionals with different amounts of Hartree-Fock exchange fraction, 0, 25 and 50%, respectively.

Not surprisingly, the separation of the KS orbital energy levels increases from 3.3 to 7.8 eV going from PBE to PBEh50. Note that, in absence of experiments, it is difficult to discern the optimal fraction of non-local exchange to use and one must rely on trends. The values predicted by applying the one-shot the G_0W_0 on the top of PBE, PBE0 and PBEh50 are 7.6, 8.3 and 8.8 eV,

whereas the reference Δ SCF results yielded to E_g values of 6.6, 7.7, and 8.7 eV, respectively. These data still show a certain degree of dependence, larger at Δ SCF level, on the fraction of non-local exchange included in the DFT functional. Finally, the values obtained from the partial self-consistent GW method are 9.2 (ev GW @PBE), 9.1 (ev GW @PBE0), and 8.9 eV (ev GW @PBEh50), interestingly indicating that ev GW exhibits a smaller dependence on the employed density functional than the G_0W_0 results. This does not necessarily imply, however, a more accurate description; especially in view of the discrepancies with Δ SCF method and the lack of experimental data to contrast these results. For instance, Körbel *et al.*³³ found that the G_0W_0 method provided a description of the experimental IP/EAs in small transition metal molecules, better than that arising from other self-consistent GW techniques. In any case, the matching between ev GW @PBEh50 and Δ SCF@PBEh50 is remarkable but also probably misleading since such a large amount of non-local exchange will largely overestimate the band gap of bulk WO_3 (\approx 3.2 eV, see Figure S3). It is also worth noting that similar E_g trends are reported for the hexagonal $(WO_3)_{12}$ and spherical $(WO_3)_{19}$ NPs as shown in Figures S4 and S5 reported in the Supporting Information (SI).

Establishing the DFT-GW protocol on a representative NPs subset

Unfortunately, the computational burden for calculations with hybrid functionals and GW methods makes the study of realistic WO_3 NPs unaffordable. As a matter of fact, the electronic structure of large NPs composed by thousands of atoms can be figured out only at the standard DFT level. The idea that we develop in this section is, thus, trying to estimate the electronic properties (E_g , EA, IP) at a higher level of theory (GW and/or Δ SCF) by performing affordable GGA calculations.

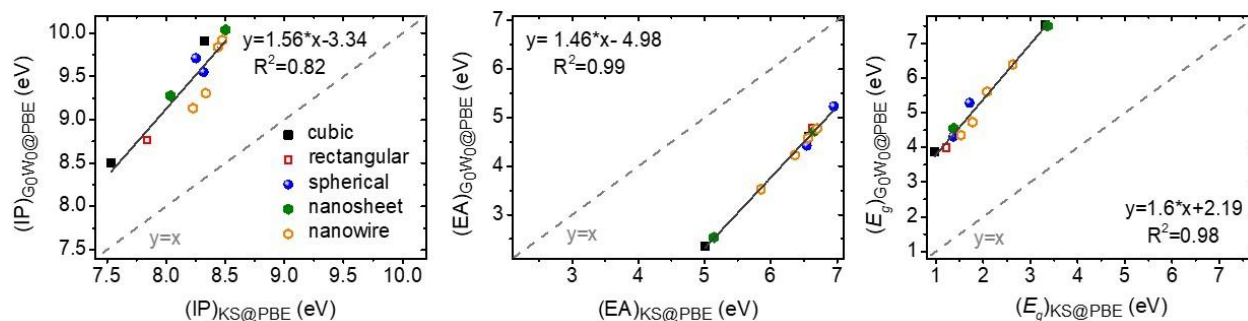


Figure 4. Correlations between the IPs, EAs and E_g (from the left to the right) for the eleven smallest NPs depicted in Figure 1, which have been calculated at the $G_0W_0@PBE$ vs $KS@PBE$.

To this end, we investigated the correlation between the three electronic quantities of interest obtained from the PBE KS orbital energies with the corresponding $G_0W_0@PBE$ values (Figure 4). This seems a logical choice since GW allows one to go from the orbital energies to the QPs which have a well-defined physical meaning. The comparison, presented in Figure 4, is carried out for the subset of eleven smaller NPs which covers all possible morphologies: two cubic, one rectangular, two spherical, two nanosheet and four nanowire NPs. This strategy allows to discard possible deviations arising from the use of a given morphology. Moreover, it also permits to compare the properties of the largest NPs with the experimental band edge energies of the monoclinic bulk phase.⁶⁸ We rely on the one shot G_0W_0 approximation that has been shown to provide excellent agreement with the experimental data for a large number of tested molecules⁶³ and is still accessible for the size of the NPs composing the selected subset. These correlations showed a nearly perfect linear dependence between the EA and E_g values estimated by both levels of theory, whereas IP quantities were slightly diverging from the linear behaviour. Similar trends were found in the correlations between $\Delta SCF@PBE$ and $KS@PBE$ (see Figure S7).

Predicting the electronic properties over the full set on NPs

Figure 5 presents the estimated DFT- GW values of the IP, EA and E_g for all NPs studied in this work, as obtained by applying the grey line correlations of Figure 4 to the quantities calculated at PBE level. The corresponding quantities estimated at $\Delta\text{SCF}@PBE0$ and $\Delta\text{SCF}@PBE$ are reported in Figure S9. Note that the systematic deviation of IPs, EAs and on their corresponding gaps predicted by GW and ΔSCF methods are qualitatively similar (see Figure S8). Thus, the agreement in the trends followed by the IP/EA energies with the NP size estimated from either $G_0W_0@PBE$, $\Delta\text{SCF}@PBE$ and $\Delta\text{SCF}@PBE0$ is remarkable (see Figure S9). Therefore, even if any of the three methods can be used to investigate trends with size and since PBE0 clearly overestimates the E_g in WO_3 , we find it convenient to henceforth focus on the $G_0W_0@PBE$ estimates only. Note that in the following discussion we will make use of the terms IP/EA and conduction/valence band (CB/VB) edges to depict the frontier energy levels of the NPs and bulk materials, respectively.

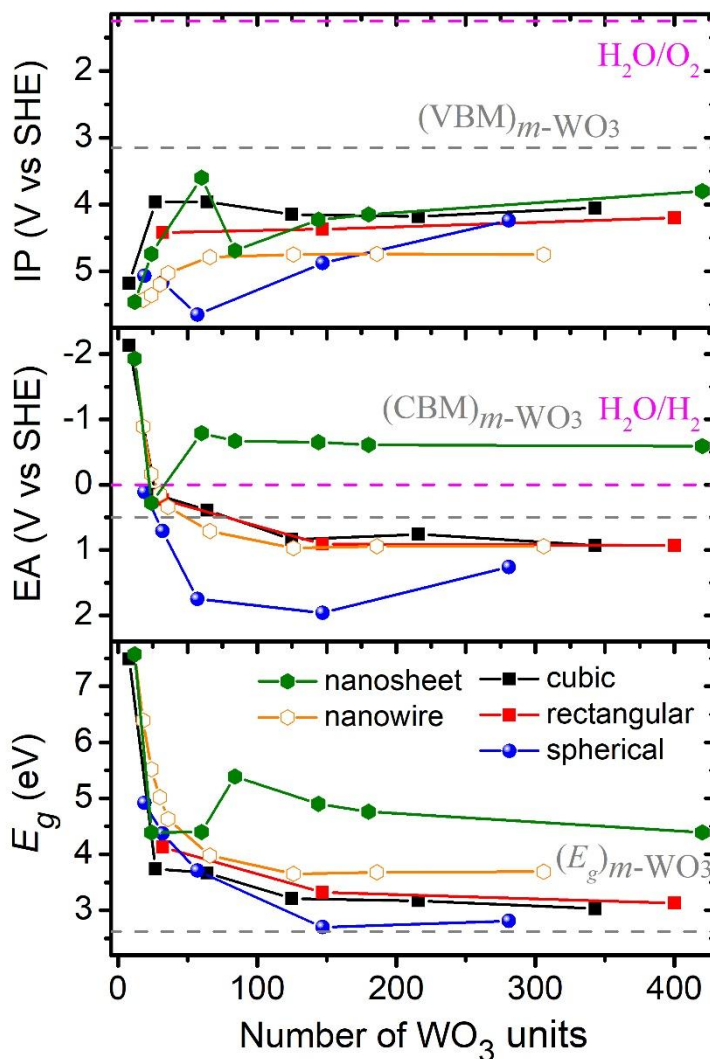


Figure 5. Ground EA, IP, E_g energies as function of their number of chemical units for the monoclinic cubic, rectangular, spherical, and for the hexagonal nanosheets and nanowire NPs; as estimated from the correlation between $KS@PBE$ and $G_0W_0@PBE$ in Figure 4. Note that the Standard Hydrogen Evolution (SHE) potential has been employed as a reference to plot the IP/EA energies.

Interestingly, the plots in Figure 5 indicate that the IP of the WO₃ NPs do not so strongly vary with the size or the morphology of the NP as compared with their EAs, lying in a range 4-5.5 V vs SHE. Indeed, both estimates are in a rather fair agreement and appear to significantly

overestimate the experimental VB edge (*i.e.*, 3.1 V vs SHE).⁶⁸ On the other hand, the EAs exhibit a significant drop in energy when going below the 100 units and, what is more interesting, they show a large dependence on the NP morphology. While cubic, rectangular and nanowire NPs display an identical behaviour with respect to the NPs size (leading to converged EA values of 0.9 V vs SHE), nanosheet NPs present EA values lower than those of the rest of NP families (with converged energies about -0.7 V vs SHE). Comparing these quantities to the monoclinic WO₃ CB energy of 0.5 V vs SHE⁶⁸ and the H₂/H₂O reduction potential (0V vs SHE), it appears that the electron injection driving forces with respect to this potential are significantly reduced when decreasing the NP size, with the exception of the nanosheet NPs. Remarkably, the stronger impact of the quantum confinement effects in the EA with respect the IP energies has been observed also experimentally observed,³⁸ where a change of 1.02 eV in the CB edge was found when moving from bulk phase to quantum dots, whereas this shift only amounted by 0.57 eV for the VB.

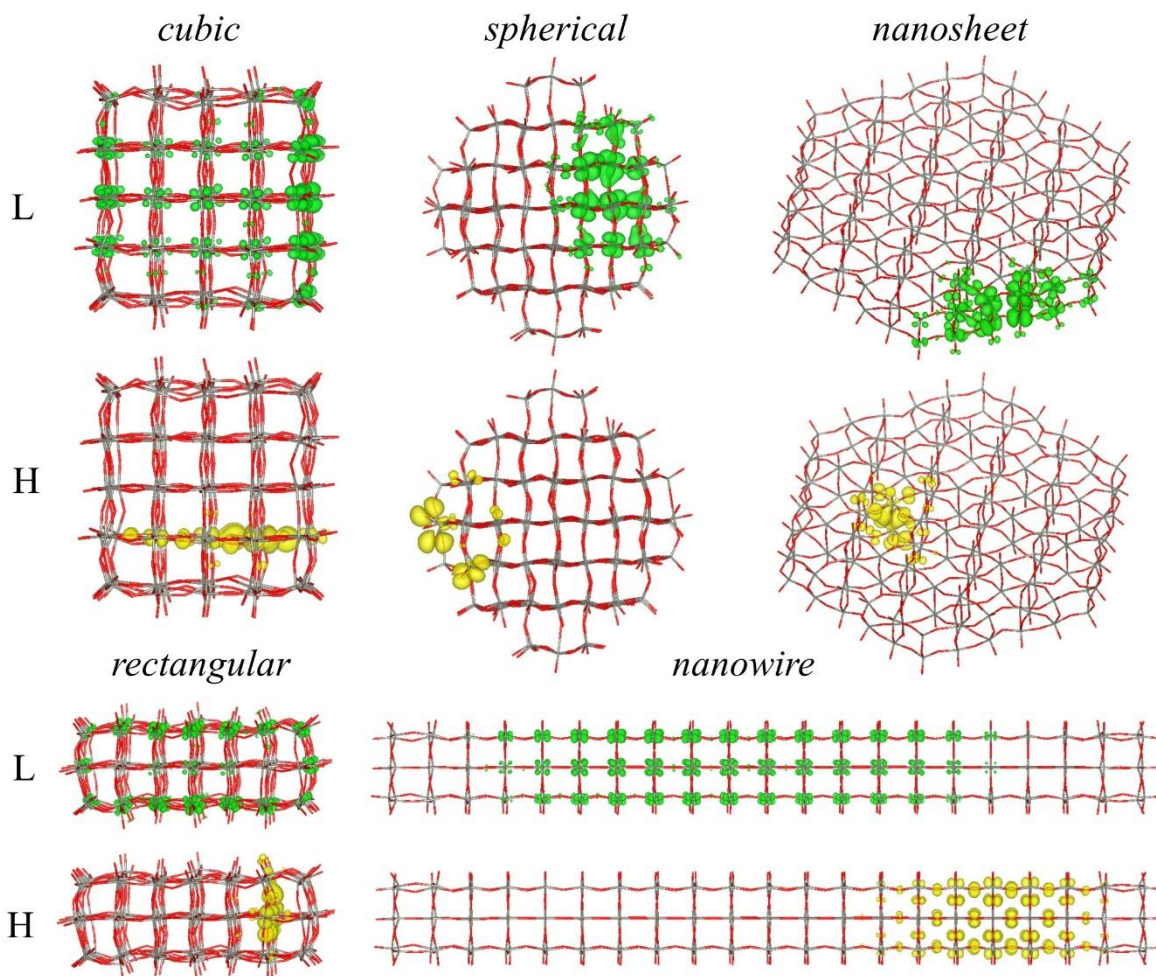


Figure 6. Isodensity plots of the HOMO (yellow) and LUMO (green) for the $(\text{WO}_3)_{125}$ cubic, $(\text{WO}_3)_{147}$ rectangular, $(\text{WO}_3)_{147}$ spherical, $(\text{WO}_3)_{144}$ nanosheet and $(\text{WO}_3)_{126}$ nanowire NPs; as calculated at the PBE level of theory. We used an isovalue equal to $3 \cdot 10^{-3}$ a.u.

To get a deeper understanding of the different behaviour of IP and EA energies with the NP size and morphology, we have plotted, in Figure 6, the frontier MOs (HOMO/LUMO) of a representative medium size NP of each family owing a comparable number of chemical units composed by 500-600 atoms. For all the families the HOMO KS orbital is highly localized over a few full coordinated oxygen atoms, essentially dominated by the O(2p) orbitals. As a result, the dependence of the HOMO localization with the NP sizes is almost negligible, as shown by the

similar IP energies calculated for all series of NPs. On the contrary, LUMO KS orbitals are fully delocalized on W atoms and mostly dominated by the $5d$ orbitals of W atoms located at the NP surfaces, thus implying a stronger impact of the size and morphology of the NP. Regarding the evolution of E_g , which seems to stabilise at around 150 WO_3 units, all families of NPs present a significant reduction of the gap as the NP size increases. This gap decreasing ranked from 7.5 eV for the smallest NPs to converged gap values for the monoclinic NPs about 2.7-3.5 eV, which are in excellent agreement with the measured (2.62 eV)⁶⁹ and calculated gaps at $G_0W_0@LDA$ (2.92 eV)⁷⁰ and at the PBE0 (3.72 eV, see Figure S3) levels of theory for the monoclinic WO_3 bulk. To sum up, we can set to 150 the critical number of chemical units where the quantum confinement effects start to be important for WO_3 NPs. Nevertheless, a significant increase in E_g values can be detrimental for the photoactivity of the material, since small NPs featuring an E_g larger than 3 eV will absorb light in the UV region, thus covering a narrow portion of the solar spectrum. In this viewpoint, by taking as a reference the experimental value of the E_g (2.62 eV), we can state that those NPs which exhibit a E_g lower than 0.4 eV with respect to their asymptotic value will still work in the VIS region. By looking at the data plotted in Figure 5, we can conclude that all NPs which possess a number of chemical units larger than ca. 100 to satisfy this condition ($(E_g)_n - (E_g)_\infty < 0.4$ eV). On overall, these results indicate that the NPs presenting a number of chemical units lying in the interval of $100 < n < 150$ are likely to display an excellent photocatalytic behavior. This corresponds to sizes of $a= 1.4-1.8$ nm for cubic; $a=2.1-2.4$ nm, $c=0.7-0.8$ nm for the rectangular; $a=2.4-2.7$ nm for spherical; $R=7.2-9.5$ for nanosheet; and $R= 8.5-13$ for nanowire NPs. These unprecedented results, obtained from a reliable state-of-the-art DFT-GW protocol, clearly show the urgent need to have fine control over the size of the

synthesized NPs to enhance the photoactivity of the material and open the door to exploit the smallest NPs for wide gap absorption applications.

Conclusions

In this work we have established a solid theoretical protocol, based on combining DFT and state-of-the-art GW calculations to investigate the intertwined role played by the size and morphology of realistic WO_3 NPs on the relevant opto-electronic properties which drive its photocatalytic behaviour. The first addressed issue was the relative stability for the different NP morphologies as the size of the NP increases. We found that cubic/nanosheet NPs are energetically favoured for medium and large size monoclinic/hexagonal phase NPs, while, for small NPs ($n < 50/125$), rectangular/nanowire NPs displayed a larger stability. In all the cases the NPs energies reached an asymptotic dependency with their size for a few hundred of units. Then, we investigated their optoelectronic properties, showing that the proper description of the electron injection/extraction energies can be achieved only if the QP correction to the KS orbital energies is applied through a GW approach or by invoking the Δ SCF method, although the choice of the exchange-correlation remains an open issue. Nevertheless, for a representative subset of NPs a linear correlation emerges between KS orbital energies and either $G_0W_0@PBE$ or Δ SCF@PBE0 calculated values of IP and EA indicating that the error in the KS orbital energies is systematic. Next, by making use of these correlations we were able to obtain EA/IP energies of $G_0W_0@PBE$ quality for all the set of NPs studied in this work. The high localization of the highest occupied levels on few oxygen atoms of the NP was found to be at the origin of the almost independent behaviour of the IP energies with respect the size and morphology of the NP. On the other hand, a large delocalization over the whole NP of the LUMO on the $5d$ W orbitals induced a large dependence of EAs upon size and morphology, with a sizeable drop in magnitudes when moving to small NP

sizes ($n < 100$). The present results indicate that the photocatalytic efficiency of WO_3 nanostructures for water oxidation can be substantially improved by quantum confinement effects when moving towards nanocrystals below about 150 units of WO_3 and choosing the proper morphology.

This is the first time that the structure and electronic properties of a complete set of realistic-size WO_3 NPs, spanning all phases and morphologies experimentally reported, are systematically investigated by high level DFT and large-scale GW calculations. We argue that these results may serve as a basis to encourage the experimental community working in photocatalysis to dedicate more research efforts in the synthesis and characterization of small-sized WO_3 NPs which could benefit from the quantum confinement effects. From a theoretical and computational viewpoint, the WO_3 nanocluster models developed in this work can be used to study charge generation and dynamics within the NPs, as well as investigate the mechanism of the water oxidation reaction, addressing finite size and surface effects; whereas our DFT- GW based method can be extended to the study of other relevant materials for photocatalysis, such as ZnO or SnO_2 NPs.

ASSOCIATED CONTENT

Supporting Information

The Supporting Information is available free of charge on the ACS Publications website. Tests for the relativistic effects, calculated gaps for the monoclinic bulk, one electron energy diagrams for hexagonal $(\text{WO}_3)_{12}$ and spherical $(\text{WO}_3)_{19}$ NPs, method correlations for the eleven smallest NPs, and evolution of IP, EA and E_g energies with the NP size for the ΔSCF methods.

AUTHOR INFORMATION

Corresponding Authors

Valentin Diez-Cabanes- *Université de Lorraine & CNRS, Laboratoire de Physique et Chimie Théoriques (LPCT), UMR 7019, F-54000, Nancy, France* ORCID: <https://orcid.org/0000-0002-6234-2749>. Email: valentin.diez-cabanes@univ-lorraine.fr

Angel Morales-Garcia- *Departament de Ciència de Materials i Química Física & Institut de Química Teòrica i Computacional (IQTUB), Universitat de Barcelona, c/Martí i Franqués 1-11, 08028 Barcelona, Spain* ORCID: <https://orcid.org/0000-0003-0491-1234>. Email: angel.morales@ub.edu

Mariachiara Pastore- *Université de Lorraine & CNRS, Laboratoire de Physique et Chimie Théoriques (LPCT), UMR 7019, F-54000, Nancy, France.* ORCID: <https://orcid.org/0000-0003-4793-1964>. Email: mariachiara.pastore@univ-lorraine.fr

Authors

Francesc Illas- *Departament de Ciència de Materials i Química Física & Institut de Química Teòrica i Computacional (IQTUB), Universitat de Barcelona, c/Martí i Franqués 1-11, 08028 Barcelona, Spain* ORCID: <https://orcid.org/0000-0003-2104-6123>.

Notes

The authors declare no competing financial interest.

ACKNOWLEDGMENT

V.D.-C. is grateful to the financial support given by the COMETE project (COncEption in silico de Matériaux pour l'Environnement et l'Energie), which is co-funded by the European Union under the program 'FEDER-FSE Lorraine et Massif des Vosges 2014-2020. M.P. acknowledges

ANR JCJC HELIOSH2 (ANR-17-CE05-0007-01) project for the financial support. The work carried out at the Universitat de Barcelona has been supported by the Spanish MICIUN RTI2018-095460-B-I00 and María de Maeztu MDM-2017-0767 grants, and, in part, by Generalitat de Catalunya 2017SGR13 grant and COST Action CA18234. A.M.-G. is thankful to the Juan de la Cierva Incorporación Programme grant IJCI-2017-31979 and F.I. acknowledges additional support from the 2015 ICREA Academia Award for Excellence in University Research. Computational resources were provided by the mésocentre EXPLOR of Université de Lorraine (Project 2018CPMXX0602), the LPCT local computational resources, and the Très Grand Centre de Calcul du CEA (TGCC) facilities. We also thank to the resources supplied by the Red Española de Supercomputacion (RES) under the grant QS-2020-2-0008, and by the HPC-Europa3 Transnational Access programme project number HPC17N1MY8.

References

- (1) Gupta, N. M. Factors Affecting the Efficiency of a Water Splitting Photocatalyst: A Perspective. *Renew. Sustain. Energy Rev.* **2017**, *71*, 585–601.
- (2) Wang, S.; Liu, G.; Wang, L. Crystal Facet Engineering of Photoelectrodes for Photoelectrochemical Water Splitting. *Chem. Rev.* **2019**, *119*, 5192–5247.
- (3) Osterloh, F. E. Nanoscale Effects in Water Splitting Photocatalysis. *Top Curr Chem* **2015**, *371*, 1–26.
- (4) Tong, H.; Ouyang, S.; Bi, Y.; Umezawa, N.; Oshikiri, M.; Ye, J. Nano-Photocatalytic Materials: Possibilities and Challenges. *Adv. Mater.* **2012**, *24*, 229–251.
- (5) Newton, K. A.; Osterloh, F. E. Size and Morphology of Suspended WO₃ Particles Control Photochemical Charge Carrier Extraction and Photocatalytic Water Oxidation Activity. *Top. Catal.* **2016**, *59*, 750–756.
- (6) Nunzi, F.; Mosconi, E.; Storchi, L.; Ronca, E.; Selloni, A.; Grätzel, M.; De Angelis, F. Inherent Electronic Trap States in TiO₂ Nanocrystals: Effect of Saturation and Sintering. *Energy Environ. Sci.* **2013**, *6*, 1221–1229.
- (7) Ronca, E.; Marotta, G.; Pastore, M.; De Angelis, F. Effect of Sensitizer Structure and TiO₂ Protonation on Charge Generation in Dye-Sensitized Solar Cells. *J. Phys. Chem. C* **2014**, *118*, 16927–16940.
- (8) Pastore, M.; De Angelis, F. First-Principles Modeling of a Dye-Sensitized TiO₂/IrO₂ Photoanode for Water Oxidation. *J. Am. Chem. Soc.* **2015**, *137*, 5798–5809.
- (9) Pavone, M.; Casparly Toroker, M. Toward Ambitious Multiscale Modeling of Nanocrystal Catalysts for Water Splitting. *ACS Energy Lett.* **2020**, *5*, 2042–2044.
- (10) Nakata, K.; Fujishima, A. TiO₂ Photocatalysis: Design and Applications. *J. Photochem.*

- Photobiol. C Photochem. Rev.* **2012**, *13*, 169–189.
- (11) Fujishima, A.; Rao, T. N.; Tryk, D. A. Titanium Dioxide Photocatalysis. *J. Photochem. Photobiol. C Photochem. Rev.* **2000**, *1*, 1–21.
- (12) Huang, Z. F.; Song, J.; Pan, L.; Zhang, X.; Wang, L.; Zou, J. J. Tungsten Oxides for Photocatalysis, Electrochemistry, and Phototherapy. *Adv. Mater.* **2015**, *27*, 5309–5327.
- (13) Gesheva, K.; Szekeres, A.; Ivanova, T. Optical Properties of Chemical Vapor Deposited Thin Films of Molybdenum and Tungsten Based Metal Oxides. *Sol. Energy Mater. Sol. Cells* **2003**, *76*, 563–576.
- (14) Hodes, G.; Cahen, D.; Manassen, J. Tungsten Trioxide as a Photoanode for a Photoelectrochemical Cell (PEC). *Nature* **1976**, *260*, 312–313.
- (15) Nowotny, J. *Oxide Semiconductors for Solar Energy Conversion: Titanium Dioxide*; CRC Press: Boca Raton, **2016**.
- (16) Ingham, B.; Hendy, S. C.; Chong, S. V.; Tallon, J. L. Density-Functional Studies of Tungsten Trioxide, Tungsten Bronzes, and Related Systems. *Phys. Rev. B - Condens. Matter Mater. Phys.* **2005**, *72*, 3–6.
- (17) Wang, F.; Di Valentin, C.; Pacchioni, G. Electronic and Structural Properties of WO₃: A Systematic Hybrid DFT Study. *J. Phys. Chem. C* **2011**, *115*, 8345–8353.
- (18) Ping, Y.; Rocca, D.; Galli, G. Optical Properties of Tungsten Trioxide from First-Principles Calculations. *Phys. Rev. B - Condens. Matter Mater. Phys.* **2013**, *87*, 1–8.
- (19) Hamdi, H.; Salje, E. K. H.; Ghosez, P.; Bousquet, E. First-Principles Reinvestigation of Bulk WO₃. *Phys. Rev. B* **2016**, *94*, 1–11.
- (20) Zhang, N.; Chen, C.; Mei, Z.; Liu, X.; Qu, X.; Li, Y.; Li, S.; Qi, W.; Zhang, Y.; Ye, J.; Roy, V. A. L.; Ma, R. Monoclinic Tungsten Oxide with {100} Facet Orientation and

- Tuned Electronic Band Structure for Enhanced Photocatalytic Oxidations. *ACS Appl. Mater. Interfaces* **2016**, *8*, 10367–10374.
- (21) Lee, T.; Lee, Y.; Jang, W.; Soon, A. Understanding the Advantage of Hexagonal WO₃ as an Efficient Photoanode for Solar Water Splitting: A First-Principles Perspective. *J. Mater. Chem. A* **2016**, *4*, 11498–11506.
- (22) Kishore, R.; Cao, X.; Zhang, X.; Bieberle-Hütter, A. Electrochemical Water Oxidation on WO₃ Surfaces: A Density Functional Theory Study. *Catal. Today* **2019**, *321–322*, 94–99.
- (23) Sun, Q.; Rao, B. K.; Jena, P.; Stolcic, D.; Kim, Y. D.; Gantefor, G.; Castleman, A. W. Appearance of Bulk Properties in Small Tungsten Oxide Clusters. *J. Chem. Phys.* **2004**, *121*, 9417–9422.
- (24) Di Valentin, C.; Wang, F.; Pacchioni, G. Tungsten Oxide in Catalysis and Photocatalysis: Hints from DFT. *Top. Catal.* **2013**, *56*, 1404–1419.
- (25) Morales-García, Á.; Macià Escatllar, A.; Illas, F.; Bromley, S. T. Understanding the Interplay between Size, Morphology and Energy Gap in Photoactive TiO₂ Nanoparticles. *Nanoscale* **2019**, *11*, 9032–9041.
- (26) Morales-García, Á.; Valero, R.; Illas, F. Reliable and Computationally Affordable Prediction of the Energy Gap of (TiO₂): N ($10 \leq n \leq 563$) Nanoparticles from Density Functional Theory. *Phys. Chem. Chem. Phys.* **2018**, *20*, 18907–18911.
- (27) Lamiel-Garcia, O.; Ko, K. C.; Lee, J. Y.; Bromley, S. T.; Illas, F. When Anatase Nanoparticles Become Bulklike: Properties of Realistic TiO₂ Nanoparticles in the 1-6 Nm Size Range from All Electron Relativistic Density Functional Theory Based Calculations. *J. Chem. Theory Comput.* **2017**, *13*, 1785–1793.
- (28) Viñes, F.; Lamiel-Garcia, O.; Illas, F.; Bromley, S. T. Size Dependent Structural and

- Polymorphic Transitions in ZnO: From Nanocluster to Bulk. *Nanoscale* **2017**, *9*, 10067–10074.
- (29) Reining, L. The GW Approximation: Content, Successes and Limitations. *Wiley Interdiscip. Rev. Comput. Mol. Sci.* **2018**, *8*, 1–26.
- (30) Berardo, E.; Kaplan, F.; Bhaskaran-Nair, K.; Shelton, W. A.; Van Setten, M. J.; Kowalski, K.; Zwijnenburg, M. A. Benchmarking the Fundamental Electronic Properties of Small TiO₂ Nanoclusters by GW and Coupled Cluster Theory Calculations. *J. Chem. Theory Comput.* **2017**, *13*, 3814–3828.
- (31) Morales-García, Á.; Valero, R.; Illas, F. Performance of the G₀W₀ Method in Predicting the Electronic Gap of TiO₂ Nanoparticles. *J. Chem. Theory Comput.* **2017**, *13*, 3746–3753.
- (32) Morales-García, Á.; Valero, R.; Illas, F. Electronic Properties of Realistic Anatase TiO₂ Nanoparticles from G₀W₀ Calculations on a Gaussian and Plane Waves Scheme. *J. Chem. Theory Comput.* **2019**, *15*, 5024–5030.
- (33) Körbel, S.; Boulanger, P.; Duchemin, I.; Blase, X.; Marques, M. A. L.; Botti, S. Benchmark Many-Body GW and Bethe-Salpeter Calculations for Small Transition Metal Molecules. *J. Chem. Theory Comput.* **2014**, *10*, 3934–3943.
- (34) Lamiel-Garcia, O.; Cuko, A.; Calatayud, M.; Illas, F.; Bromley, S. T. Predicting Size-Dependent Emergence of Crystallinity in Nanomaterials: Titania Nanoclusters: Versus Nanocrystals. *Nanoscale* **2017**, *9*, 1049–1058.
- (35) Houx, N. Le; Pourroy, G.; Camerel, F.; Comet, M.; Spitzer, D. WO₃ Nanoparticles in the 5-30 Nm Range by Solvothermal Synthesis under Microwave or Resistive Heating. *J. Phys. Chem. C* **2010**, *114*, 155–161.

- (36) Tanaka, D.; Oaki, Y.; Imai, H. Enhanced Photocatalytic Activity of Quantum-Confined Tungsten Trioxide Nanoparticles in Mesoporous Silica. *Chem. Commun.* **2010**, *46*, 5286–5288.
- (37) Watanabe, H.; Fujikata, K.; Oaki, Y.; Imai, H. Band-Gap Expansion of Tungsten Oxide Quantum Dots Synthesized in Sub-Nano Porous Silica. *Chem. Commun.* **2013**, *49*, 8477–8479.
- (38) Cong, S.; Tian, Y.; Li, Q.; Zhao, Z.; Geng, F. Single-Crystalline Tungsten Oxide Quantum Dots for Fast Pseudocapacitor and Electrochromic Applications. *Adv. Mater.* **2014**, *26*, 4260–4267.
- (39) Wang, S.; Kershaw, S. V.; Li, G.; Leung, M. K. H. The Self-Assembly Synthesis of Tungsten Oxide Quantum Dots with Enhanced Optical Properties. *J. Mater. Chem. C* **2015**, *3*, 3280–3285.
- (40) Xie, Y. P.; Liu, G.; Yin, L.; Cheng, H. M. Crystal Facet-Dependent Photocatalytic Oxidation and Reduction Reactivity of Monoclinic WO₃ for Solar Energy Conversion. *J. Mater. Chem.* **2012**, *22*, 6746–6751.
- (41) D'Arienzo, M.; Armelao, L.; Mari, C. M.; Polizzi, S.; Ruffo, R.; Scotti, R.; Morazzoni, F. Surface Interaction of WO₃ Nanocrystals with NH₃. Role of the Exposed Crystal Surfaces and Porous Structure in Enhancing the Electrical Response. *RSC Adv.* **2014**, *4*, 11012–11022.
- (42) Zhao, Z. G.; Liu, Z. F.; Miyauchi, M. Nature-Inspired Construction, Characterization, and Photocatalytic Properties of Single-Crystalline Tungsten Oxide Octahedra. *Chem. Commun.* **2010**, *46*, 3321–3323.
- (43) Ding, J.; Chai, Y.; Liu, Q.; Liu, X.; Ren, J.; Dai, W. L. Selective Deposition of Silver

- Nanoparticles onto WO₃ Nanorods with Different Facets: The Correlation of Facet-Induced Electron Transport Preference and Photocatalytic Activity. *J. Phys. Chem. C* **2016**, *120*, 4345–4353.
- (44) Lin, R.; Wan, J.; Xiong, Y.; Wu, K.; Cheong, W. C.; Zhou, G.; Wang, D.; Peng, Q.; Chen, C.; Li, Y. Quantitative Study of Charge Carrier Dynamics in Well-Defined WO₃ Nanowires and Nanosheets: Insight into the Crystal Facet Effect in Photocatalysis. *J. Am. Chem. Soc.* **2018**, *140*, 9078–9082.
- (45) Perdew, J. P.; Burke, K.; Ernzerhof, M. Generalized Gradient Approximation Made Simple. *Phys. Rev. Lett.* **1996**, *77*, 3865–3868.
- (46) Hutter, J.; Iannuzzi, M.; Schiffmann, F.; Vandevondele, J. Cp2k: Atomistic Simulations of Condensed Matter Systems. *Wiley Interdiscip. Rev. Comput. Mol. Sci.* **2014**, *4*, 15–25.
- (47) Goedecker, S.; Teter, M. Separable Dual-Space Gaussian Pseudopotentials. *Phys. Rev. B - Condens. Matter Mater. Phys.* **1996**, *54*, 1703–1710.
- (48) Blum, V.; Gehrke, R.; Hanke, F.; Havu, P.; Havu, V.; Ren, X.; Reuter, K.; Scheffler, M. Ab Initio Molecular Simulations with Numeric Atom-Centered Orbitals. *Comput. Phys. Commun.* **2009**, *180*, 2175–2196.
- (49) Chang, C.; Pelissier, M.; Durand, P. Regular Two-Component Pauli-like Effective Hamiltonians in Dirac Theory. *Phys. Scr.* **1986**, *34*, 394–404.
- (50) Van Lenthe, E.; Baerends, E. J.; Snijders, J. G. Relativistic Regular Two-Component Hamiltonians. *J. Chem. Phys.* **1993**, *99*, 4597–4610.
- (51) Adamo, C.; Barone, V. Toward Reliable Density Functional Methods without Adjustable Parameters: The PBE0 Model. *J. Chem. Phys.* **1999**, *110*, 6158–6170.
- (52) Bredas, J. L. Mind the Gap! *Mater. Horizons* **2014**, *1*, 17–19.

- (53) Kohn, W.; Sham, L. J. Self-Consistent Equations Including Exchange and Correlation Effects. *Phys. Rev.* **1965**, *140*, 1133–1138.
- (54) Kohn, W. Nobel Lecture: Electronic Structure of Matter—Wave Functions and Density Functionals. *Rev. Mod. Phys.* **1999**, *71*, 1253–1266.
- (55) Hedin, L. New Method for Calculating the One-Particle Green's Function with Application to the Electron-Gas Problem. *Phys. Rev.* **1965**, *139*, 796–823.
- (56) Onida, G.; Reining, L.; Rubio, A. Electronic Excitations: Density-Functional versus Many-Body Green's-Function Approaches. *Rev. Mod. Phys.* **2002**, *74*, 601–659.
- (57) Kronik, L.; Stein, T.; Refaely-Abramson, S.; Baer, R. Excitation Gaps of Finite-Sized Systems from Optimally Tuned Range-Separated Hybrid Functionals. *J. Chem. Theory Comput.* **2012**, *8*, 1515–1531.
- (58) Sun, H.; Autschbach, J. Electronic Energy Gaps for π -Conjugated Oligomers and Polymers Calculated with Density Functional Theory. *J. Chem. Theory Comput.* **2014**, *10*, 1035–1047.
- (59) Perdew, J. P. Density Functional Theory and the Band Gap Problem. *Int. J. Quantum Chem.* **1985**, *28*, 497–523.
- (60) Morales-García, Á.; Valero, R.; Illas, F. An Empirical, yet Practical Way to Predict the Band Gap in Solids by Using Density Functional Band Structure Calculations. *J. Phys. Chem. C* **2017**, *121*, 18862–18866.
- (61) Li, W.; Walther, C. F. J.; Kuc, A.; Heine, T. Density Functional Theory and beyond for Band-Gap Screening: Performance for Transition-Metal Oxides and Dichalcogenides. *J. Chem. Theory Comput.* **2013**, *9*, 2950–2958.
- (62) Hai, X.; Tahir-Kheli, J.; Goddard, W. A. Accurate Band Gaps for Semiconductors from

- Density Functional Theory. *J. Phys. Chem. Lett.* **2011**, *2*, 212–217.
- (63) Van Setten, M. J.; Caruso, F.; Sharifzadeh, S.; Ren, X.; Scheffler, M.; Liu, F.; Lischner, J.; Lin, L.; Deslippe, J. R.; Louie, S. G.; Yang, C.; Weigend, F.; Neaton, J. B.; Evers, F.; Rinke, P. GW100: Benchmarking G0W0 for Molecular Systems. *J. Chem. Theory Comput.* **2015**, *11*, 5665–5687.
- (64) Rinke, P.; Qteish, A.; Neugebauer, J.; Scheffler, M. Exciting Prospects for Solids: Exact-Exchange Based Functionals Meet Quasiparticle Energy Calculations. *Phys. Status Solidi Basic Res.* **2008**, *245*, 929–945.
- (65) Bruneval, F.; Marques, M. A. L. Benchmarking the Starting Points of the GW Approximation for Molecules. *J. Chem. Theory Comput.* **2013**, *9* (1), 324–329.
- (66) Ren, X.; Rinke, P.; Blum, V.; Wieferink, J.; Tkatchenko, A.; Sanfilippo, A.; Reuter, K.; Scheffler, M. Resolution-of-Identity Approach to Hartree-Fock, Hybrid Density Functionals, RPA, MP2 and GW with Numeric Atom-Centered Orbital Basis Functions. *New J. Phys.* **2012**, *14*, 0–55.
- (67) Johnston, R. L. *Atomic and Molecular Clusters*; CRC Press: London, **2002**.
- (68) Grätzel, M. Photoelectrochemical Cells. *Nature* **2001**, *414*, 338–344.
- (69) Gullapalli, S. K.; Vemuri, R. S.; Ramana, C. V. Structural Transformation Induced Changes in the Optical Properties of Nanocrystalline Tungsten Oxide Thin Films. *Appl. Phys. Lett.* **2010**, *96*, 20–23.
- (70) Johansson, M. B.; Baldissera, G.; Valyukh, I.; Persson, C.; Arwin, H.; Niklasson, G. A.; Österlund, L. Electronic and Optical Properties of Nanocrystalline WO₃ Thin Films Studied by Optical Spectroscopy and Density Functional Calculations. *J. Phys. Condens. Matter* **2013**, *25*, 205502.

